Comput Mech (2012) 50:789–804
DOI 10.1007/s00466-012-0781-z

ORIGINAL PAPER

Immersed smoothed finite element method for fluid–structure interaction simulation of aortic valves

Jianyao Yao · G. R. Liu · Daria A. Narmoneva · Robert B. Hinton · Zhi-Qian Zhang

Received: 19 July 2012 / Accepted: 11 August 2012 / Published online: 4 September 2012

Abstract This paper presents a novel numerical method for simulating the fluid–structure interaction (FSI) problems when blood flows over aortic valves. The method uses the immersed boundary/element method and the smoothed finite element method and hence it is termed as IS-FEM. The IS-FEM is a partitioned approach and does not need a body-fitted mesh for FSI simulations. It consists of three main modules: the fluid solver, the solid solver and the FSI force solver. In this work, the blood is modeled as incompressible viscous flow and solved using the characteristic-based-split scheme with FEM for spacial discretization. The leaflets of the aortic valve are modeled as Mooney-Rivlin hyperelastic materials and solved using smoothed finite element method (or S-FEM). The FSI force is calculated on the Lagrangian fictitious fluid mesh that is identical to the moving solid mesh. The octree search and neighbor-to-neighbor schemes are used to detect efficiently the FSI pairs of fluid and solid cells. As an example, a 3D idealized model of aortic valve is modeled, and the opening process of the valve is simulated using the proposed IS-FEM. Numerical results indicate that the IS-FEM can serve as an efficient tool in the study of aortic valve dynamics to reveal the details of stresses in the aortic valves, the flow velocities in the blood, and the shear forces on the interfaces. This tool can also be applied to animal models studying disease processes and may ultimately translate to a new adaptive methods working with magnetic resonance images, leading to improvements on diagnostic and prognostic paradigms, as well as surgical planning, in the care of patients.

Keywords Fluid–structure interaction · Immersed smoothed finite element method · Fictitious fluid · Characteristic-based split · Aortic valve

J. Yao (✉) · G. R. Liu
School of Aerospace Systems, College of Engineering and Applied Science, University of Cincinnati, Cincinnati, OH, USA
e-mail: yaojy@ucmail.uc.edu

G. R. Liu
e-mail: liugr@ucmail.uc.edu

D. A. Narmoneva
Department of Biomedical Engineering, University of Cincinnati, Cincinnati, OH, USA

R. B. Hinton
Division of Cardiology, The Heart Institute, Cincinnati Children's Hospital Medical Center, Cincinnati, OH, USA

Z.-Q. Zhang
Singapore-MIT Alliance (SMA), National University of Singapore, 117576 Singapore, Singapore

1 Introduction

Valvular heart disease is a significant cause of morbidity and mortality world-wide. Since the left heart bears a significantly higher pressure load than the right heart, leading to extremely large deformations, diseases of the left-sided aortic and mitral valves are more common. The total annual mortality due to valvular heart diseases is more than 20,000 patients per year in the United States alone [1–3]. Extrapolating current trends, it is predicted that about 800,000 people worldwide will require heart valve replacement annually by the year 2020 [4], which creates substantial medical and financial burdens, including for example prosthetic mechanical or biological valve production. One proposed solution to this problem is that valves should be repaired rather than replaced whenever possible [5,6], a practice currently reserved for a minority of select cases. An effective repair strategy requires a complete understanding on the cyclic stress level on the valves and the aortic walls supporting the valves. Presently,

these dynamics are poorly understood, and not taken into consideration in a clinical context. Therefore, carefully devised computational approaches capable of capturing the dynamics of heart valves coupled with the hemodynamics, i.e., a fluid–structure interaction (FSI) simulation enabled heart valve solver, will advance clinical decision making paradigms and ultimately improve valve disease treatments. In addition, it enables engineers to design effective mechanical or biological valves for replacement solutions [7].

A simplified simulation of aortic valve dynamics is a purely structural analysis [8–11] which produces the deformation and strain/stress distribution on leaflets by applying a uniform pressure load on the appropriate surfaces. The assumption of uniform pressure load ignores the distribution of the normal and shear stresses acting on the valvular structures induced by the hemodynamics and its effects on the valve dynamics. However, the leaflets of aortic valve are very thin and soft, and hence the interaction between the blood and valvular structures could be very intense and the results obtained by purely structural analysis could be questionable in many cases. Therefore, the FSI analysis of aortic valve is necessary to obtain more accurate pressure distribution during the dynamic cardiac cycle.

Currently, there are two kinds of method for the FSI simulations, moving-mesh method, which include the arbitrary Lagrangian–Eulerian (ALE) schemes [12,13] and the space-time (ST) method [14–17], and the immersed-type methods. The moving-mesh schemes have been known to be accurate, suitable for both compressible and incompressible flows, and can be used for almost all the cases of FSI simulations. However, a mesh update method uses a mesh that is moving and re-meshed. A number of mesh moving methods [18–21] that reduce the frequency of remeshing have been developed for FSI computations, including FSI problems with large displacement [20]. Computations that involve contact between structural surfaces, though challenging, can also be computed with moving mesh methods, provided that the physics of the problem does not require the precise computation of the flow through the gap between the contacting surfaces (and bringing that the flow to zero when there is the actual contact). Examples of that are 3D fluid–particle interaction computations with 1,000 spheres falling in a liquid filled tube [22], with a remeshing frequency that was only about every 10 time steps, and very complex parachute FSI computations in 3D [23], with large deformations of the parachute canopy, and with contact between the parachutes of a cluster of parachutes. However, if the precise value of the gap is important (which is the case of aortic valves), then the moving-mesh method would be more difficult to use. Therefore, although the moving-mesh methods are the most commonly used in FSI studies [24,25], including the arterial FSI [26–29], it has not yet been successfully applied to valve models due to the frequent contact between the structural surfaces. Nevertheless, the moving-mesh is still used in commercial software for aortic valve dynamics, regardless the efficiency [29–31].

The most commonly used method for FSI simulations of aortic valve is the immersed-type methods, including immersed boundary method (IBM) [32–35] and fictitious domain (FD) approach [36–38]. For the FSI problems, the IBM couples an Eulerian description of the fluid (no body-fitted mesh is needed) to a Lagrangian description of the immersed structure. The interaction between fluid and structure variables is mediated by integral transformation with Dirac delta function kernels at the interface. The structure part is modeled as elastic fibers which resist extension, compression, and bending. One major disadvantage of the IBM is that the elastic fiber assumption limits accurate representation of immersed flexible structure within the fluid domain. Thus, the FSI simulations using IBM emphasize more on the fluid part to predict the blood flow across prosthetic mechanical valves or natural valves.

The fluid and structure part are also solved independently in FD method. This approach is based on the imposition of velocity constraints associated with moving boundaries by means of Lagrange multipliers [36]. The basic idea of the FD method is to extend the fluid problem defined in real physical fluid domain (exclude the immersed structure) to a problem defined in the whole computation domain (the sum of real physical domain of both fluid and structure), while still forcing the velocity boundary conditions. However, similar as the IBM, one major limitation of the FD method lies in the modeling of structure part. Although the structure part is modeled as the Neo-Hookean material in [37,38], the body forces and the inertia terms are neglected during FSI computation.

The immersed finite element method (IFEM) [39–41] provides an approach to overcome the modeling problems of structure part in both IBM and FD method. With finite element formulations for both fluid and solid domain, the submerged structure is solved more realistically and accurately. The key idea of the IFEM is to regard the fluid and solid as one continuum, leading to a unique way for deriving the physical FSI force. The interaction is realized by interpolating the FSI force from solid to fluid, and interpolating the velocity from fluid back to solid. Unlike the IBM or FD methods where the interaction occurs along the interface of the two domains, the interpolation takes place on the whole overlapping domain. A possible disadvantage of IFEM is that the accuracy may be dependent on the mesh size ratio between the fluid and solid domain since it could affect the interpolation of FSI force.

As inspired by the above mentioned immersed-type methods, a novel *Immersed Smoothed Finite Element Method* (IS-FEM) [42,43] is developed for FSI simulation. In the IS-FEM, the fluid and structure is discretized using T-type mesh (triangular for 2D and tetrahedral for 3D) and solved independently, and the fictitious fluid is introduced for evaluating interaction between fluid and structure. Unlike the IFEM, the

interaction is realized by interpolating velocity from structure to fluid, and interpolating pressure from fluid to fictitious fluid which has the same configuration as structure to calculate the FSI force. We will introduce the interaction process in detail in the following sections.

There are several distinguished features of the newly developed IS-FEM making it extremely suitable for FSI simulations of aortic valve, which has complex geometry and very large movement of soft and incompressible tissues (leaflets). First, the T-type mesh has much better adaptation to complicated geometry than the other types of mesh. Second, the use of S-FEM [44–46] improves the accuracy of standard FEM by overcome the "overly stiff" phenomenon and provides a stable and efficient way (named smoothing-domain-based selective FS/NS-FEM-T4 model [45,46]) to remove volumetric locking in nearly incompressible solids. Third, the use of FD makes the interaction process more accurate, robust and insensitive to the mesh size ratio between fluid and structure.

In this paper, a 3D version of IS-FEM is developed for the FSI simulation of aortic valves. The blood is modeled as the isothermal incompressible viscous flow and solved using the characteristic-based-split (CBS) algorithm [47–49]. The leaflets of aortic valve are modeled as isotropic nearly incompressible Mooney-Rivlin hyperelastic material and solved using explicit time integration based on central difference algorithm. The paper has five more sections. In Sect. 2, the governing equations of the FSI systems with fictitious fluid domain are briefly summarized. The structural solver based on S-FEM and explicit time integration is described in Sect. 3. The detailed procedure for IS-FEM is presented in Sect. 4. In Sect. 5, an ideal aortic valve is modeled and its FSI simulations are carried out using the proposed IS-FEM. The conclusions are drawn in the last section.

2 Governing equations of IS-FEM

2.1 Fictitious domain and FSI force

In this section, we will give the governing equations for the general 3D FSI problems, which describe a moving and deformable solid body with a finite volume fully immerses in incompressible viscous fluid flow. As shown in Fig. 1a, the function $\chi(\mathbf{X}^{\mathrm{s}}, t)$ describes the solid changing from the initial configuration ${}^{0}\Omega^{\mathrm{s}}$ at time $t = 0$ to the current configuration Ω^{s} at time t. The material and spatial coordinates of the solid particles are denoted by $\mathbf{X}^{\mathrm{s}}$ and $\mathbf{x}^{\mathrm{s}}$, respectively. The real fluid domain is denoted by Ω^{f}, which is not overlapped with Ω^{s} but attached at the fluid–solid interface Γ^{fs}. Γ^{fs} is a part of the boundary of Ω^{f} and is naturally identical to the closed boundary Γ^{s} of Ω^{s}. In the real FSI system, no fluid exists in the volume which the solid Ω^{s} occupies. Due to the

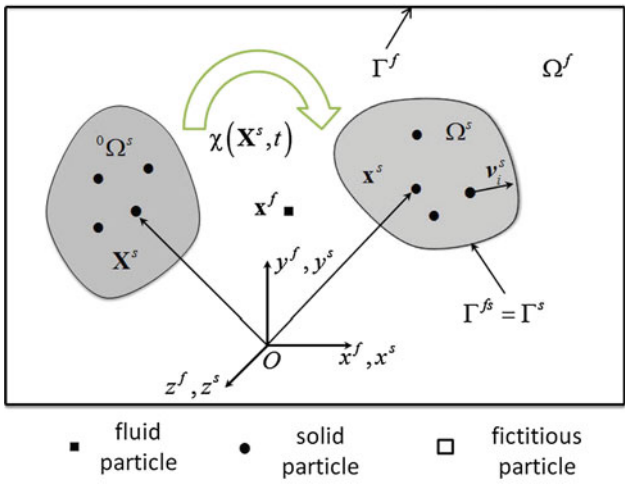

(a) Configurations of fluid and solid domains

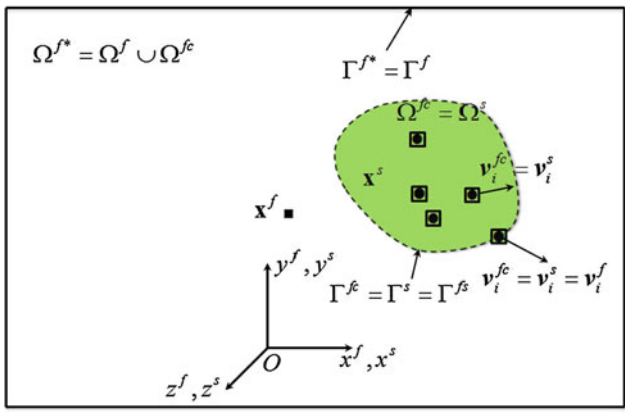

(b) Configuration of fictitious fluid domain

Fig. 1 Illustration of fluid, structure and fictitious domains

motion of the solid, Ω^{f} and Ω^{s} are time-varying domains. In this paper, the superscripts "f" and "s" denote fluid and solid/structure, respectively.

With the assumption of conventional non-slip condition on the fluid–solid interface Γ^{fs}, the equations of motion of fluid and solid can be written as:

$$\begin{cases} \rho^{\mathrm{f}} \dfrac{\mathrm{D}v_i^{\mathrm{f}}}{\mathrm{D}t} = \mathrm{div}\sigma_{ij}^{\mathrm{f}} + \rho^{\mathrm{f}} g_i, \ \mathbf{x}^{\mathrm{f}} \in \Omega^{\mathrm{f}} \\ \rho^{\mathrm{s}} \dfrac{\mathrm{D}v_i^{\mathrm{s}}}{\mathrm{D}t} = \mathrm{div}\sigma_{ij}^{\mathrm{s}} + \rho^{\mathrm{s}} g_i, \ \mathbf{x}^{\mathrm{s}} \in \Omega^{\mathrm{s}} \\ v_i^{\mathrm{f}} = v_i^{\mathrm{s}}, \qquad \text{on } \Gamma^{\mathrm{fs}} \\ f_i^{\mathrm{s,FSI}} = -f_i^{\mathrm{f,FSI}}, \qquad \text{on } \Gamma^{\mathrm{fs}} \end{cases} \tag{1}$$

where ρ denotes the density, v_i the velocity, and σ_{ij} the Cauchy stress. For three-dimensional problems, $i, j = 1, 2, 3$. The boundary conditions for the fluid and structure unrelated to the FSI are omitted for the sake of simplicity. The local form of FSI force exerted on the fluid particles $\mathbf{x}^{\mathrm{f}} \in \Gamma^{\mathrm{fs}}$can be determined as follows,

$$f_i^{\mathrm{f,FSI}} = \rho^{\mathrm{f}} \frac{\mathrm{D}v_i^{\mathrm{f}}}{\mathrm{D}t} - \mathrm{div}\sigma_{ij}^{\mathrm{f}} - \rho^{\mathrm{f}} g_i, \ \text{with } v_i^{\mathrm{f}} = v_i^{\mathrm{s}} \text{ on } \Gamma^{\mathrm{fs}} \tag{2}$$

where σ_{ij}^{f} is calculated using the velocity $v_i^{\mathrm{f}} = v_i^{\mathrm{s}}$ on FSI boundary Γ^{fs}. If Γ^{fs} can be explicitly depicted for the fluid, the calculation of FSI force is quite straightforward. However, Γ^{fs} is implicit and time-varying in the immersed-type methods, and thus require a proper way to evaluate the FSI force.

In order to employ the numerical methods using Eulerian mesh and coordinates to solve the fluid flow, we have to construct a time-independent computational fluid domain, which satisfies the governing equations in Eq. (1). For this purpose, we introduce a fictitious fluid domain $\Omega^{\mathrm{fc}} = \Omega^{\mathrm{s}}$ with a closed boundary $\Gamma^{\mathrm{fc}} = \Gamma^{\mathrm{s}} = \Gamma^{\mathrm{fs}}$, as shown in Fig. 1b. Ω^{fc} is filled with the so-called fictitious fluid, which is incompressible viscous fluid in this research. During the FSI process, the equations of motion of the fictitious fluid can be written in the same form as Eq. (1):

$$\rho^{\mathrm{fc}} \frac{\mathrm{D}v_i^{\mathrm{fc}}}{\mathrm{D}t} = \mathrm{div}\sigma_{ij}^{\mathrm{fc}} + \rho^{\mathrm{fc}} g_i + f_i^{\mathrm{fc}}, \quad \mathbf{x}^{\mathrm{fc}} \in \Omega^{\mathrm{fc}} \quad \left(\Omega^{\mathrm{fc}} = \Omega^{\mathrm{s}}\right) \tag{3}$$

Here, an additional body force f_i^{fc} is given to balance the momentum equation. In the above equation, the properties of fictitious fluid and the continuous velocity field need to be determined. Thus, we add two assumptions to the fictitious flow:

(1) The fictitious fluid is assumed to have the same properties as the real fluid, i.e., we have $\rho^{\mathrm{fc}} = \rho^{\mathrm{f}}$ for density, and $\mu^{\mathrm{fc}} = \mu^{\mathrm{f}}$ for the dynamic viscosity. This assumption makes the domain $\Omega^{\mathrm{f}*} = \Omega^{\mathrm{f}} \cup \Omega^{\mathrm{fc}}$ filled with the homogeneous fluid.
(2) The fictitious fluid particles are assumed to be "bounded" to the solid particles all the time, as shown in Fig. 1b. This assumption gives the velocity field $v_i^{\mathrm{fc}} = v_i^{\mathrm{s}}$ for the fictitious fluid in Ω^{fc}. Obviously, we have $v_i^{\mathrm{fc}} = v_i^{\mathrm{s}} = v_i^{\mathrm{f}}$ on the boundary Γ^{fc}, leading to a continuous velocity field in the domain $\Omega^{\mathrm{f}*}$.

Under the second assumption, the motion of the fictitious fluid particles is enforced to be consistent with that of the bounded solid particles. Hence, a pair of action and reaction forces arises, denoted by $f_i^{\mathrm{f,FSI}}$ and $f_i^{\mathrm{s,FSI}}$. $f_i^{\mathrm{f,FSI}}$ works as a body force replacing f_i^{fc} in Eq. (3) as follows,

$$f_i^{\mathrm{f,FSI}} = \rho^{\mathrm{fc}} \frac{\mathrm{D}v_i^{\mathrm{fc}}}{\mathrm{D}t} - \mathrm{div}\sigma_{ij}^{\mathrm{fc}} - \rho^{\mathrm{fc}} g_i, \qquad \text{with } v_i^{\mathrm{fc}} = v_i^{\mathrm{s}} \text{ in } \Omega^{\mathrm{fc}} \tag{4}$$

It should be noted that the FSI force in Eq. (4) is defined in Ω^{fc}, which is different from the FSI force in Eq. (2) defined only on Γ^{fc}. The equation of motion of the fictitious fluid in the integral form can be written as

$$\begin{cases} \int_{\Omega^{\mathrm{fc}}} \rho^{\mathrm{f}} \dfrac{\mathrm{D}v_i^{\mathrm{fc}}}{\mathrm{D}t} \mathrm{d}\Omega = \int_{\Omega^{\mathrm{fc}}} \mathrm{div}\sigma_{ij}^{\mathrm{fc}} \mathrm{d}\Omega + \int_{\Omega^{\mathrm{fc}}} \rho^{\mathrm{f}} g_i \mathrm{d}\Omega + F_i^{\mathrm{f,FSI}} \\ v_i^{\mathrm{fc}} = v_i^{\mathrm{s}}, \text{ in } \Omega^{\mathrm{fc}} \end{cases} \tag{5}$$

where

$$F_i^{\mathrm{f,FSI}} = \int_{\Omega^{\mathrm{fc}}} f_i^{\mathrm{f,FSI}} \mathrm{d}\Omega \tag{6}$$

Combined with the integral form of equation of motion for real fluid, we have

$$\begin{aligned} &\int_{\Omega^{\mathrm{f}}} \rho^{f} \frac{\mathrm{D}v_i^{\mathrm{f}}}{\mathrm{D}t} \mathrm{d}\Omega + \int_{\Omega^{\mathrm{fc}}} \rho^{\mathrm{f}} \frac{\mathrm{D}v_i^{\mathrm{fc}}}{\mathrm{D}t} \mathrm{d}\Omega = \int_{\Omega^{\mathrm{f}}} \mathrm{div}\sigma_{ij}^{\mathrm{f}} \mathrm{d}\Omega + \int_{\Omega^{\mathrm{fc}}} \mathrm{div}\sigma_{ij}^{\mathrm{fc}} \mathrm{d}\Omega \\ &\quad + \int_{\Omega^{\mathrm{f}}} \rho^{\mathrm{f}} g_i \mathrm{d}\Omega + \int_{\Omega^{\mathrm{fc}}} \rho^{\mathrm{f}} g_i \mathrm{d}\Omega + F_i^{\mathrm{f,FSI}} \end{aligned} \tag{7}$$

Since the two domains Ω^{f} and Ω^{fc} are non-overlapping and only attached at Γ^{fc}, and filled with homogeneous fluid, the motion of equations in $\Omega^{\mathrm{f}*}$ can be expressed as

$$\begin{cases} \int_{\Omega^{\mathrm{f}*}} \rho^{\mathrm{f}} \dfrac{\mathrm{D}v_i^{\mathrm{f}*}}{\mathrm{D}t} \mathrm{d}\Omega = \int_{\Omega^{\mathrm{f}*}} \mathrm{div}\sigma_{ij}^{\mathrm{f}*} \mathrm{d}\Omega + \int_{\Omega^{\mathrm{f}*}} \rho^{\mathrm{f}} g_i \mathrm{d}\Omega + F_i^{\mathrm{f,FSI}} \\ v_i^{\mathrm{f}*} = v_i^{\mathrm{s}}, \quad \text{in } \Omega^{\mathrm{fc}} \end{cases} \tag{8}$$

And the FSI force can be calculated as

$$f_i^{\mathrm{f,FSI}} = \rho^{\mathrm{f}} \frac{Dv_i^{\mathrm{f}*}}{Dt} - \mathrm{div}\sigma_{ij}^{\mathrm{f}*} - \rho^{\mathrm{f}} g_i, \quad \text{with } v_i^{\mathrm{f}*} = v_i^{\mathrm{s}} \text{ in } \Omega^{\mathrm{fc}} \tag{9}$$

2.2 Governing equations for FSI system

According to the above discussion, we can conclude that there are three sets of equations of the proposed IS-FEM: (1) the Navier–Stokes equations for incompressible viscous flow; (2) equations of motion for nonlinear solid, which is described by total Lagrangian in this research; (3) equations for the calculation of FSI force. In the following text, the superscript "f*" is replaced by "f".

For the incompressible viscous fluid, the differential form of Navier–Stokes equations can be written as

$$\begin{cases} \dfrac{\partial v_i^{\mathrm{f}}}{\partial x_i^{\mathrm{f}}} = 0 \\ \rho^{\mathrm{f}} \dfrac{\partial v_i^{\mathrm{f}}}{\partial t} + \rho^{\mathrm{f}} \dfrac{\partial}{\partial x_j^{\mathrm{f}}} \left(v_i^{\mathrm{f}} v_j^{\mathrm{f}} \right) = -\dfrac{\partial p^{\mathrm{f}}}{\partial x_i^{\mathrm{f}}} + \dfrac{\partial \tau_{ij}^{\mathrm{f}}}{\partial x_j^{\mathrm{f}}} + \rho^{\mathrm{f}} g_i \end{cases} \tag{10}$$

where p^{f} represents the fluid pressure, and τ_{ij}^{f} is the deviatoric stresses as

$$\tau_{ij}^{\mathrm{f}} = \mu^{\mathrm{f}} \left(\frac{\partial v_i^{\mathrm{f}}}{\partial x_j^{\mathrm{f}}} + \frac{\partial v_j^{\mathrm{f}}}{\partial x_i^{\mathrm{f}}} - \frac{2}{3} \frac{\partial v_k^{\mathrm{f}}}{\partial x_k^{\mathrm{f}}} \delta_{ij} \right) \tag{11}$$

where δ_{ij} is the Kroneker delta. The boundary conditions can be described as

$$\begin{cases} g_{\mathrm{vbc}}^{\mathrm{f}}(v_i) = v_i^{\mathrm{f}} - \bar{v}_i^{\mathrm{f}} = 0, \text{ on } \Gamma_v^{\mathrm{f}} \text{ for velocity} \\ g_{\mathrm{pbc}}^{\mathrm{f}}(p) = p^{\mathrm{f}} - \bar{p}^{\mathrm{f}} = 0, \text{ on } \Gamma_p^{\mathrm{f}} \text{ for pressure} \end{cases} \tag{12}$$

and the initial conditions are

$$v_i^{\mathrm{f}} = {}^0\bar{v}_i^{\mathrm{f}}, \; p^{\mathrm{f}} = {}^0p^{\mathrm{f}} \text{ at } t = 0 \tag{13}$$

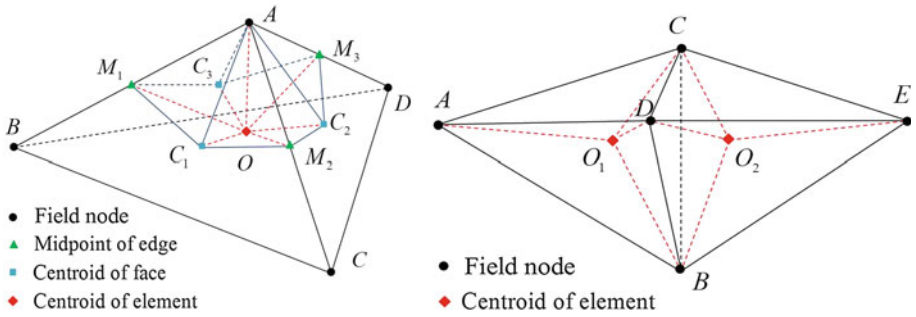

(a) node-based **(b)** face-based

Fig. 2 Illustration of node-based and face-based smoothing domain

Here, the values with $\bar{\bullet}$ denote the prescribed field variable values for boundary and initial conditions.

For the nonlinear solid, the equations of motion can be written as

$$\rho^{\mathrm{s}}\ddot{u}_i^{\mathrm{s}} = \frac{\partial P_{ji}^{\mathrm{s}}}{\partial X_j^{\mathrm{s}}} + \rho^{\mathrm{s}} g_i \tag{14}$$

where P_{ji}^{s} is the first Piola-Kirchhoff stress of the solid, and u_i^{s} and $\ddot{u}_i^{\mathrm{s}}$ are the displacement and acceleration of the solid, respectively. The boundary conditions of the solid can be written as

$$\begin{cases} n_j^{\mathrm{s}}\sigma_{ji}^{\mathrm{s}} = \bar{T}_i^{\mathrm{s}} \text{ on } \Gamma_T^{\mathrm{s}} \text{ for load/stress} \\ v_i^{\mathrm{s}} = \bar{v}_i^{\mathrm{s}} \quad \text{on } \Gamma_v^{\mathrm{s}} \text{ for velocity} \end{cases} \tag{15}$$

and the initial conditions are

$$P_{ji}^{\mathrm{s}} = {}^0\bar{P}_{ji}^{\mathrm{s}}, \text{ and } v_i^{\mathrm{s}} = {}^0\bar{v}_i^{\mathrm{s}} \text{ at } t = 0 \tag{16}$$

where Γ_T^{s} is the natural boundary of the solid with outward normal n_j^{s} and the prescribed traction force $\bar{T}_i^{\mathrm{s}}$, and Γ_v^{s} is the velocity boundary.

For the FSI force calculation, we have the conditions for velocity and forcing as

$$\begin{cases} v_i^{\mathrm{f}} = v_i^{\mathrm{s}}, & \text{in } \Omega^{\mathrm{fc}} \text{ for velocity} \\ f_i^{\mathrm{f,FSI}} = -f_i^{\mathrm{s,FSI}}, & \text{in } \Omega^{\mathrm{s}} \text{ for force} \end{cases} \tag{17}$$

and $f_i^{\mathrm{f,FSI}}$ is calculated as

$$f_i^{\mathrm{f,FSI}} = \rho^{\mathrm{f}}\frac{\partial v_i^{\mathrm{f}}}{\partial t} + \rho^{\mathrm{f}}\frac{\partial}{\partial x_j^{\mathrm{f}}}\left(v_i^{\mathrm{f}} v_j^{\mathrm{f}}\right) + \frac{\partial p^{\mathrm{f}}}{\partial x_i^{\mathrm{f}}} - \frac{\partial \tau_{ij}^{\mathrm{f}}}{\partial x_j^{\mathrm{f}}} - \rho^{\mathrm{f}} g_i, \text{ in } \Omega^{\mathrm{fc}} \tag{18}$$

In the numerical simulations, the fluid domain Ω^{f} and solid domain Ω^{s} are discretized by two different sets of meshes, respectively. These two sets of meshes are not required to coincide. It is also not necessary to adopt the same type of the element. In this work, only the simplest linear element, 4-node tetrahedral (T4) element is employed for both fluid and solid parts. Since the CBS algorithm for incompressible fluid is quite standard, we will not elaborate on that in this paper. In the following section, we will briefly introduce how to solve 3D nonlinear solid using S-FEM.

3 S-FEM for solving nonlinear solid dynamics

3.1 Overview of smoothing operation in S-FEM

For three-dimensional problems, we use 4-node tetrahedral elements to discretize the solid domain. There are two kinds of S-FEM for 3D problems: the node-based smoothed FEM (NS-FEM) and the face-based smoothed FEM (FS-FEM). The node-based smoothing domain is created by connecting the midpoint of edges, the centroid of faces, and the centroid of elements around the node of interest. A part of the node-based smoothing domain around node A is shown in Fig. 2a (the polyhedron $AM_1C_1M_2C_2M_3C_3O$), where only a partition of element $ABCD$ is plotted for clearance. The face-based smoothing domain is created by connecting the nodes of the face and the centroids of the elements on both sides of the face of interest, as shown in Fig. 2b (the polyhedron O_1BCDO_2).

For the IS-FEM, the calculation domain is discretized into $N_{\mathrm{ele}}^{\mathrm{s}}$ elements with $N_{\mathrm{n}}^{\mathrm{s}}$ nodes, and a set of non-overlapping smoothing domains are created based on the elements. The material coordinates of the solid nodes are denoted by $\mathbf{X}_{Ii}^{\mathrm{s}}$. In both FEM and S-FEM, the displacement u_i^{s} and velocity v_i^{s} are interpolated using the standard FEM procedure:

$$u_i^{\mathrm{s}} = \sum_I {}^0\Phi_I^{\mathrm{s}} u_{Ii}^{\mathrm{s}}, \quad v_i^{\mathrm{s}} = \sum_I {}^0\Phi_I^{\mathrm{s}} v_{Ii}^{\mathrm{s}} \tag{19}$$

where ${}^0\Phi_I^{\mathrm{s}}$ is the shape function calculated at the initial configuration. In S-FEM, the spatial derivatives are calculated based on the gradient smoothing method. The smoothed displacement gradient in ${}^0\Omega_i^{\mathrm{sd}}$ (which denotes the smoothing domain at initial configuration associated with a material point $\mathbf{X}_{i\mathrm{sd}}^{\mathrm{s}}$) can be expressed as:

$$\bar{u}_{i,j}^{\mathrm{s}}\left(\mathbf{X}_{i\mathrm{sd}}^{\mathrm{s}}\right) = \int_{{}^0\Omega_i^{\mathrm{sd}}} u_{i,j}^{\mathrm{s}}\left(\mathbf{X}^{\mathrm{s}}\right) W\left(\mathbf{X}^{\mathrm{s}}; \mathbf{X}^{\mathrm{s}} - \mathbf{X}_{i\mathrm{sd}}^{\mathrm{s}}\right) \mathrm{d}\Omega \tag{20}$$

where $u^{\mathrm{s}}_{i,j} = \partial u^{\mathrm{s}}_i / \partial X^{\mathrm{s}}_j$ is the gradient of the displacement field. In this research, we use the piecewise constant (Heaviside) function for the gradient smoothing operation:

$$W\left(\mathbf{X}^{\mathrm{s}}; \mathbf{X}^{\mathrm{s}} - \mathbf{X}^{\mathrm{s}}_{i\mathrm{sd}}\right) = \begin{cases} 1/V^{\mathrm{sd}}_i, & \mathbf{X}^{\mathrm{s}} \in {}^0\Omega^{\mathrm{sd}}_i \\ 0, & \mathbf{X}^{\mathrm{s}} \notin {}^0\Omega^{\mathrm{sd}}_i \end{cases} \tag{21}$$

where V^{sd}_i is the volume of the smoothing domain ${}^0\Omega^{\mathrm{sd}}_i$. Integrating Eq. (20) by part and considering Eqs. (19) and (21), we have

$$\begin{aligned} \bar{u}^{\mathrm{s}}_{i,j}\left(\mathbf{X}^{\mathrm{s}}_{i\mathrm{sd}}\right) &= \sum_I \left(\frac{1}{V^{\mathrm{sd}}_i} \int_{\Gamma^{\mathrm{sd}}_i} {}^0\Phi^{\mathrm{s}}_I\left(\mathbf{X}^{\mathrm{s}}_{i\mathrm{sd}}\right) {}^0n^{\mathrm{sd}}_j \mathrm{d}\Gamma \right) u^{\mathrm{s}}_{Ii} \\ &= \sum_I {}^0\bar{\Phi}^{\mathrm{s}}_{I,j}\left(\mathbf{X}^{\mathrm{s}}_{i\mathrm{sd}}\right) u^{\mathrm{s}}_{Ii} \end{aligned} \tag{22}$$

where ${}^0\bar{\Phi}^{\mathrm{s}}_{I,j}$ is the smoothed derivatives of shape function.

In the finite deformation analysis, the deformation gradient, $F_{ij} = u_{i,j} + \delta_{ij}$, is the primary strain measure. The smoothing operation on the deformation gradient F_{ij} yields the following smoothed deformation gradient $\bar{F}_{ij}$:

$$\bar{F}^{\mathrm{s}}_{ij} = \sum_I {}^0\bar{\Phi}^{\mathrm{s}}_{I,j}\left(\mathbf{X}^{\mathrm{s}}_{i\mathrm{sd}}\right) u^{\mathrm{s}}_{Ii} + \delta_{ij} \tag{23}$$

Using $\bar{F}_{ij}$, one can easily construct the smoothed Cauchy-Green deformation tensor, which will be shown in the following section.

Beside the smoothing operation over the strain field, the other operations of S-FEM are almost the same as the standard FEM, we will not elaborate on that in this paper.

3.2 Calculation of hyperelastic materials using S-FEM

The leaflets of aortic valve are usually modeled as rubber-like hyperelastic materials. The strain energy density function of nearly incompressible Mooney-Rivlin materials can be written as

$$W = c_{10}\left(\bar{I}_1 - 3\right) + c_{01}\left(\bar{I}_2 - 3\right) + \frac{\kappa}{2}(J-1)^2 \tag{24}$$

where c_{10} and c_{01} are empirically determined (usually fitted from experimental data), and $\bar{I}_1$, $\bar{I}_2$ and $\bar{I}_3$ are three reduced invariants of right Cauchy-Green deformation tensor $\mathbf{C} = \mathbf{F}^{\mathrm{T}}\mathbf{F}$:

$$\bar{I}_1 = I_1 I_3^{-1/3},\ \bar{I}_2 = I_2 I_3^{-2/3},\ J = I_3^{1/2} \tag{25}$$

with

$$I_1 = \mathrm{tr}\mathbf{C},\ I_2 = \frac{1}{2}\left\{(\mathrm{tr}\mathbf{C})^2 + \mathrm{tr}\left(\mathbf{C}^2\right)\right\},\ I_3 = \det(\mathbf{C}) \tag{26}$$

κ is the bulk modulus, which can be expressed as:

$$\kappa = \frac{2(c_{10} + c_{01})}{1 - 2\upsilon} \tag{27}$$

The Cauchy–Lagrangian strain tensor is defined as

$$\mathbf{E} = \frac{1}{2}(\mathbf{C} - \mathbf{I}) \tag{28}$$

The second Piola-Kirchhoff (PK2) stress can be calculated as:

$$S_{ij} = \frac{\partial W}{\partial E_{ij}} = 2\frac{\partial W}{\partial C_{ij}} \tag{29}$$

Using the strain energy density function in Eq. (24), we have

$$\begin{aligned} S_{ij} = {} & 2\left(c_{10} I_3^{-1/3} + c_{01} I_3^{-2/3} I_1\right)\delta_{ij} - 2c_{01} I_3^{-2/3} C_{ij} \\ & - \left(\frac{2}{3}c_{10} I_1 I_3^{-4/3} + \frac{4}{3}c_{10} I_2 I_3^{-5/3}\right)\left(C^{-1}\right)_{ij} \\ & + \kappa(J-1)J\left(C^{-1}\right)_{ij} \end{aligned} \tag{30}$$

The first line in the above equation denotes the deviatoric component of the stress tensor, and the second line denotes the volumetric component. For incompressible materials, the third term would vanish because $I_3 = 1$. For nearly incompressible materials, the "volumetric locking" will appear since $\upsilon \approx 0.5$.

We have known that the NS-FEM is naturally immune from volumetric locking but is overly soft. Therefore, we use the smoothing-domain-based selective FS/NS-FEM, which combines the immunity of NS-FEM and the "stiff side" of FS-FEM, to overcome the volumetric locking problem of nearly incompressible materials. In this research, we use the face-based smoothing domain to calculate the deviatoric stress in the first line of Eq. (30) and use the node-based smoothing domain to calculate the volumetric stress in the second line of Eq. (30).

The internal nodal force can be calculated from the PK2 stress in Eq. (29) as

$$\overline{\mathbf{f}^{\mathrm{int}}_I} = \int_{{}^0\Omega^{\mathrm{sd}}_i} {}^0\mathbf{B}^{\mathrm{T}}_I \{\mathbf{S}\}\, \mathrm{d}\Omega \tag{31}$$

where ${}^0\mathbf{B}_I$ is the smoothed strain-displacement matrix, and can be written as

$${}^0\mathbf{B}_I = {}^0\mathbf{B}_{I0} + {}^0\mathbf{B}_{I1} \tag{32}$$

We can see that ${}^0\mathbf{B}_I$ is the sum of two parts: ${}^0\mathbf{B}_{I0}$ denotes the initial state and ${}^0\mathbf{B}_{I1}$ denotes the increment during deformation. Both ${}^0\mathbf{B}_{I0}$ and ${}^0\mathbf{B}_{I1}$ are block matrices with the following forms:

$$\begin{cases} {}^0\mathbf{B}_{I0} = \left[{}^0\mathbf{B}^{J_1}_{I0}, \ldots, {}^0\mathbf{B}^{J_{ns}}_{I0}\right] \\ {}^0\mathbf{B}_{I1} = \left[{}^0\mathbf{B}^{J_1}_{I1}, \ldots, {}^0\mathbf{B}^{J_{ns}}_{I1}\right] \end{cases} \tag{33}$$

where J_i denotes the ith supporting node of the smoothing domain, and ns is the number of supporting nodes. If the

strain is denoted as $\boldsymbol{\varepsilon} = \{\varepsilon_x \ \varepsilon_y \ \varepsilon_z \ \varepsilon_{yz} \ \varepsilon_{xz} \ \varepsilon_{xy}\}^{\mathrm{T}}$, for the ith block, we have

$$
{}^0\mathbf{B}_{I0}^{J_i} = \begin{bmatrix}
\dfrac{\partial^0\bar{\Phi}^{\mathrm{s}}_{J_i}}{\partial X^{\mathrm{s}}} & 0 & 0 \\
0 & \dfrac{\partial^0\bar{\Phi}^{\mathrm{s}}_{J_i}}{\partial Y^{\mathrm{s}}} & 0 \\
0 & 0 & \dfrac{\partial^0\bar{\Phi}^{\mathrm{s}}_{J_i}}{\partial Z^{\mathrm{s}}} \\
0 & \dfrac{\partial^0\bar{\Phi}^{\mathrm{s}}_{J_i}}{\partial Z^{\mathrm{s}}} & \dfrac{\partial^0\Phi^{\mathrm{s}}_{J_i}}{\partial Y^{\mathrm{s}}} \\
\dfrac{\partial^0\bar{\Phi}^{\mathrm{s}}_{J_i}}{\partial Z^{\mathrm{s}}} & 0 & \dfrac{\partial^0\Phi^{\mathrm{s}}_{J_i}}{\partial X^{\mathrm{s}}} \\
\dfrac{\partial^0\bar{\Phi}^{\mathrm{s}}_{J_i}}{\partial Y^{\mathrm{s}}} & \dfrac{\partial^0\bar{\Phi}^{\mathrm{s}}_{J_i}}{\partial X^{\mathrm{s}}} & 0
\end{bmatrix} \tag{34}
$$

$$
{}^0\mathbf{B}_{I1}^{J_i} = \begin{bmatrix}
\dfrac{\partial^0\bar{\Phi}^{\mathrm{s}}_{J_i}}{\partial X^{\mathrm{s}}}\dfrac{\partial x^{\mathrm{s}}_{J_i}}{\partial X^{\mathrm{s}}} & \dfrac{\partial^0\bar{\Phi}^{\mathrm{s}}_{I}}{\partial X^{\mathrm{s}}}\dfrac{\partial y^{\mathrm{s}}_{J_i}}{\partial X^{\mathrm{s}}} & \dfrac{\partial^0\bar{\Phi}^{\mathrm{s}}_{I}}{\partial X^{\mathrm{s}}}\dfrac{\partial z^{\mathrm{s}}_{J_i}}{\partial X^{\mathrm{s}}} \\
\dfrac{\partial^0\bar{\Phi}^{\mathrm{s}}_{I}}{\partial Y^{\mathrm{s}}}\dfrac{\partial x^{\mathrm{s}}_{J_i}}{\partial Y^{\mathrm{s}}} & \dfrac{\partial^0\bar{\Phi}^{\mathrm{s}}_{I}}{\partial Y^{\mathrm{s}}}\dfrac{\partial y^{\mathrm{s}}_{J_i}}{\partial Y^{\mathrm{s}}} & \dfrac{\partial^0\bar{\Phi}^{\mathrm{s}}_{I}}{\partial Y^{\mathrm{s}}}\dfrac{\partial z^{\mathrm{s}}_{J_i}}{\partial Y^{\mathrm{s}}} \\
\dfrac{\partial^0\bar{\Phi}^{\mathrm{s}}_{I}}{\partial Z^{\mathrm{s}}}\dfrac{\partial x^{\mathrm{s}}_{J_i}}{\partial Z^{\mathrm{s}}} & \dfrac{\partial^0\bar{\Phi}^{\mathrm{s}}_{I}}{\partial Z^{\mathrm{s}}}\dfrac{\partial y^{\mathrm{s}}_{J_i}}{\partial Z^{\mathrm{s}}} & \dfrac{\partial^0\bar{\Phi}^{\mathrm{s}}_{I}}{\partial Z^{\mathrm{s}}}\dfrac{\partial z^{\mathrm{s}}_{J_i}}{\partial Z^{\mathrm{s}}} \\
\dfrac{\partial^0\bar{\Phi}^{\mathrm{s}}_{I}}{\partial Y^{\mathrm{s}}}\dfrac{\partial x^{\mathrm{s}}_{J_i}}{\partial Z^{\mathrm{s}}} + \dfrac{\partial^0\bar{\Phi}^{\mathrm{s}}_{I}}{\partial Z^{\mathrm{s}}}\dfrac{\partial x^{\mathrm{s}}_{J_i}}{\partial Y^{\mathrm{s}}} & \dfrac{\partial^0\bar{\Phi}^{\mathrm{s}}_{I}}{\partial Y^{\mathrm{s}}}\dfrac{\partial y^{\mathrm{s}}_{J_i}}{\partial Z^{\mathrm{s}}} + \dfrac{\partial^0\bar{\Phi}^{\mathrm{s}}_{I}}{\partial Z^{\mathrm{s}}}\dfrac{\partial y^{\mathrm{s}}_{J_i}}{\partial Y^{\mathrm{s}}} & \dfrac{\partial^0\bar{\Phi}^{\mathrm{s}}_{I}}{\partial Y^{\mathrm{s}}}\dfrac{\partial z^{\mathrm{s}}_{J_i}}{\partial Z^{\mathrm{s}}} + \dfrac{\partial^0\bar{\Phi}^{\mathrm{s}}_{I}}{\partial Z^{\mathrm{s}}}\dfrac{\partial z^{\mathrm{s}}_{J_i}}{\partial Y^{\mathrm{s}}} \\
\dfrac{\partial^0\bar{\Phi}^{\mathrm{s}}_{I}}{\partial X^{\mathrm{s}}}\dfrac{\partial x^{\mathrm{s}}_{J_i}}{\partial Z^{\mathrm{s}}} + \dfrac{\partial^0\bar{\Phi}^{\mathrm{s}}_{I}}{\partial Z^{\mathrm{s}}}\dfrac{\partial x^{\mathrm{s}}_{J_i}}{\partial X^{\mathrm{s}}} & \dfrac{\partial^0\bar{\Phi}^{\mathrm{s}}_{I}}{\partial X^{\mathrm{s}}}\dfrac{\partial y^{\mathrm{s}}_{J_i}}{\partial Z^{\mathrm{s}}} + \dfrac{\partial^0\bar{\Phi}^{\mathrm{s}}_{I}}{\partial Z^{\mathrm{s}}}\dfrac{\partial y^{\mathrm{s}}_{J_i}}{\partial X^{\mathrm{s}}} & \dfrac{\partial^0\bar{\Phi}^{\mathrm{s}}_{I}}{\partial X^{\mathrm{s}}}\dfrac{\partial z^{\mathrm{s}}_{J_i}}{\partial Z^{\mathrm{s}}} + \dfrac{\partial^0\bar{\Phi}^{\mathrm{s}}_{I}}{\partial Z^{\mathrm{s}}}\dfrac{\partial z^{\mathrm{s}}_{J_i}}{\partial X^{\mathrm{s}}} \\
\dfrac{\partial^0\bar{\Phi}^{\mathrm{s}}_{I}}{\partial X^{\mathrm{s}}}\dfrac{\partial x^{\mathrm{s}}_{J_i}}{\partial Y^{\mathrm{s}}} + \dfrac{\partial^0\bar{\Phi}^{\mathrm{s}}_{I}}{\partial Y^{\mathrm{s}}}\dfrac{\partial x^{\mathrm{s}}_{J_i}}{\partial X^{\mathrm{s}}} & \dfrac{\partial^0\bar{\Phi}^{\mathrm{s}}_{I}}{\partial X^{\mathrm{s}}}\dfrac{\partial y^{\mathrm{s}}_{J_i}}{\partial Y^{\mathrm{s}}} + \dfrac{\partial^0\bar{\Phi}^{\mathrm{s}}_{I}}{\partial Y^{\mathrm{s}}}\dfrac{\partial y^{\mathrm{s}}_{J_i}}{\partial X^{\mathrm{s}}} & \dfrac{\partial^0\bar{\Phi}^{\mathrm{s}}_{I}}{\partial X^{\mathrm{s}}}\dfrac{\partial z^{\mathrm{s}}_{J_i}}{\partial Y^{\mathrm{s}}} + \dfrac{\partial^0\bar{\Phi}^{\mathrm{s}}_{I}}{\partial Y^{\mathrm{s}}}\dfrac{\partial z^{\mathrm{s}}_{J_i}}{\partial X^{\mathrm{s}}}
\end{bmatrix} \tag{35}
$$

with $x^{\mathrm{s}}_{J_i}$, $y^{\mathrm{s}}_{J_i}$ and $z^{\mathrm{s}}_{J_i}$ denote the displacement of supporting node J_i in x-, y-, and z-direction, respectively.

4 Procedures for IS-FEM

There are three major steps for the FSI simulation using IS-FEM, the fluid solver, the structure solve, and the FSI force calculation. In this section, we will give the sketches of the three parts.

4.1 CBS for incompressible fluid flow

There are three steps in CBS method. In the first step, the pressure term from the momentum equation will be dropped and an intermediate velocity will be calculated. In the second step, the pressure will be updated in an implicit form. In the third step, the intermediate velocity will be corrected using the pressure terms. In CBS, the velocity v_i^{f} and pressure p^{f} are interpolated using the standard FEM procedure

$$
v_i^{\mathrm{f}} = \sum_I \Phi_I^{\mathrm{f}} v_{Ii}^{\mathrm{f}}, \quad p^f = \sum_I \Phi_I^{\mathrm{f}} p_I^{\mathrm{f}} \tag{36}
$$

where Φ_I^{f} is the shape function of the fluid node I. Since the immersed S-FEM is used, the spatial discretization of fluid domain is unvarying during computation. The temporal discretization of CBS for incompressible fluids can be summarized as following.

Step I: on the intermediate momentum calculation

$$
\begin{aligned}
M_{IJ}^{\mathrm{f}} \frac{{}^*v_{Ji}^{\mathrm{f}} - {}^n v_{Ji}^{\mathrm{f}}}{\Delta t} &= -{}^n C_{IJ}^{\mathrm{f}}\, {}^n v_{Ji}^{\mathrm{f}} \\
&\quad - \frac{\Delta t}{2} {}^n K_{IJ}^{\mathrm{f}}\, {}^n v_{Ji}^{\mathrm{f}} - {}^n F_{Ii}^{\mathrm{f}} + {}^n f_{Ii}^{\mathrm{f},\tau} + {}^n f_{Ii}^{\mathrm{f},g} \\
&= {}^* RHS_{Ii}^{\mathrm{f}} + {}^n f_{Ii}^{\mathrm{f},g}
\end{aligned} \tag{37}
$$

Step II: on the pressure calculation

$$
H_{IJ}^{\mathrm{f}}\, {}^{n+1} p_J^{\mathrm{f}} = -\frac{1}{\Delta t} Q_{IJi}^{\mathrm{f}}\, {}^* v_{Ji}^{\mathrm{f}} \tag{38}
$$

Step III: on the momentum correction

$$
\begin{aligned}
M_{IJ}^{\mathrm{f}} \frac{{}^{n+1} v_{Ji}^{\mathrm{f}} - {}^n v_{Ji}^{\mathrm{f}}}{\Delta t} &= {}^{n+1} RHS_{Ii}^{\mathrm{f}} \\
&= M_{IJ}^{\mathrm{f}} \frac{{}^* v_{Ji}^{\mathrm{f}} - {}^n v_{Ji}^{\mathrm{f}}}{\Delta t} - G_{IJi}^{\mathrm{f}}\, {}^{n+1} p_J^{\mathrm{f}}
\end{aligned} \tag{39}
$$

where

$$
\begin{aligned}
&M_{IJ}^{\mathrm{f}} = \int_{\Omega^{\mathrm{f}}} \rho^{\mathrm{f}} \Phi_I^{\mathrm{f}} \Phi_J^{\mathrm{f}} \mathrm{d}\Omega, \quad {}^n C_{IJ}^{\mathrm{f}} = \int_{\Omega^{\mathrm{f}}} \rho^{\mathrm{f}} \Phi_I^{\mathrm{f}} \frac{\partial \left({}^n v_j^{\mathrm{f}} \Phi_J^{\mathrm{f}} \right)}{\partial x_j^{\mathrm{f}}} \mathrm{d}\Omega, \\
&{}^n K_{IJ}^{\mathrm{f}} = \int_{\Omega^{\mathrm{f}}} \frac{\partial \left({}^n v_k^{\mathrm{f}} \Phi_J^{\mathrm{f}} \right)}{\partial x_k^{\mathrm{f}}} \rho^{\mathrm{f}} \frac{\partial \left({}^n v_j^{\mathrm{f}} \Phi_J^{\mathrm{f}} \right)}{\partial x_j^{\mathrm{f}}} \mathrm{d}\Omega, \quad {}^n F_{Ii}^{\mathrm{f}} = \int_{\Omega^{\mathrm{f}}} \frac{\partial \Phi_J^{\mathrm{f}}}{\partial x_j^{\mathrm{f}}} {}^n \tau_{ij}^{\mathrm{f}} \mathrm{d}\Omega, \\
&{}^n f_{Ii}^{\mathrm{f},\tau} = \int_{\Gamma^{\mathrm{f}}} \Phi_I^{\mathrm{f}} {}^n \tau_{ij}^{\mathrm{f}} n_j^{\mathrm{f}} \mathrm{d}\Gamma, \quad {}^n f_{Ii}^{\mathrm{f},\tau} = \int_{\Omega^{\mathrm{f}}} \Phi_I^{\mathrm{f}} \rho^{\mathrm{f}} g_i \mathrm{d}\Omega, \\
&H_{IJ}^{\mathrm{f}} = \int_{\Omega^{\mathrm{f}}} \frac{\partial \Phi_I^{\mathrm{f}}}{\partial x_i^{\mathrm{f}}} \frac{\partial \Phi_J^{\mathrm{f}}}{\partial x_i^{\mathrm{f}}} \mathrm{d}\Omega, \quad Q_{IJi}^{\mathrm{f}} = \int_{\Omega^{\mathrm{f}}} \rho^{\mathrm{f}} \Phi_I^{\mathrm{f}} \frac{\partial \Phi_J^{\mathrm{f}}}{\partial x_i^{\mathrm{f}}} \mathrm{d}\Omega, \\
&G_{IJi}^{\mathrm{f}} = \int_{\Omega^{\mathrm{f}}} \Phi_I^{\mathrm{f}} \frac{\partial \Phi_J^{\mathrm{f}}}{\partial x_i^{\mathrm{f}}} \mathrm{d}\Omega
\end{aligned} \tag{40}
$$

The matrices M^{f}_{IJ} and H^{f}_{IJ} are invariant during computation and only need to assemble once at the beginning. The mass matrix M^{f}_{IJ} in the above equations is lumped. The pressure in step II is solved using preconditioned conjugate gradient (PCG) scheme. The above semi-implicit CBS algorithm is conditionally stable, and the critical time step is determined by

$$\Delta t_{\mathrm{cr}} = \min\left(\frac{h}{|\mathbf{u}|}, \frac{h^2}{\upsilon}\right) \tag{41}$$

where h is the size of the smallest element and υ is the kinematic viscosity.

4.2 Dynamics of nonlinear solids

In this research, the central difference method is used for the explicit time integration for nonlinear solids. For the FSI simulation of aortic valves, the equations of motion at time step n for leaflets can be written as

$$\mathbf{M}^{\mathrm{s}}\ddot{\mathbf{u}}^{\mathrm{s}} = \mathbf{f}^{\mathrm{ext}}\left(\mathbf{u}^{\mathrm{s}}, {}^{n}t\right) - \mathbf{f}^{\mathrm{int}}\left(\mathbf{u}^{\mathrm{s}}, {}^{n}t\right) \tag{42}$$

where $\mathbf{f}^{\mathrm{ext}}$ and $\mathbf{f}^{\mathrm{int}}$ denote the nonlinear external and internal nodal force. For the aortic valve, we have

$$\mathbf{f}^{\mathrm{ext}}\left(\mathbf{u}^{\mathrm{s}}, {}^{n}t\right) = \mathbf{f}^{\mathrm{s,FSI}}\left(\mathbf{u}^{\mathrm{s}}, {}^{n}t\right) + \mathbf{f}^{\mathrm{s,contact}}\left(\mathbf{u}^{\mathrm{s}}, {}^{n}t\right) \tag{43}$$

where $\mathbf{f}^{\mathrm{s,contact}}\left(\mathbf{u}^{\mathrm{s}}, {}^{n}t\right)$ denotes the contact force due to the interaction between leaflets during moving. It should be noted that contact force considered here is only used to prevent penetrations between leaflets. Therefore, only the normal contact force is calculated, and the tangential contact force (friction force) is neglected.

The implementation of central difference method is quite standard and simple, and we will not elaborate on that here. We can see the most critical parts of explicit solid dynamics are the calculations of the internal and external nodal forces. The calculation of internal nodal forces is introduced in Sect. 3.1 (see Eq. (31)), and the calculation of external nodal forces, i.e., the FSI forces, will be introduced in the following section.

4.3 FSI procedure

In Sect. 2, we have made it clear that the interaction between fluid and structure is realized via the fictitious fluid domain, which is identical to the current configuration of the structure. Thus, the solution scheme for IS-FEM could be divided into three main modules: (1) solving solid part with FSI force conditions, i.e., $f_i^{\mathrm{s,FSI}} = -f_i^{\mathrm{f,FSI}}$; (2) solving fluid part with FSI velocity conditions, i.e., $v_i^{\mathrm{f}} = v_i^{\mathrm{s}}$, for $\mathbf{x} \in \Omega^{\mathrm{fc}}$; and (3) identifying the FSI conditions.

4.3.1 Calculation of FSI forces

According to Eqs. (3) and (18), the FSI force can be obtained by solving the fictitious fluid domain ${}^{n+1}\Omega^{\mathrm{fc}}$ which uses the same spatial discretization as the solid part at current configuration ${}^{n+1}\Omega^{\mathrm{s}}$. Since the fictitious fluids have the same properties as real fluids, we can use the same CBS scheme to solve the N-S equations. In standard CBS, we calculate the fluid variables at ${}^{n+1}t$ from the variables at ${}^{n}t$ and the corresponding boundary conditions. But when we calculate $f_i^{\mathrm{f,FSI}}$ from Eq. (18), the fluid variables at both ${}^{n}t$ and ${}^{n+1}t$ in ${}^{n+1}\Omega^{\mathrm{fc}}$ are already known from the calculation of the whole fluid domain $\Omega^{\mathrm{f}*}$. The nodal velocities are determined from the assumption that the fictitious fluid particles are always bonded to the corresponding solid particles, thus we have ${}^{n+1}v^{\mathrm{fc}}_{Ii} = {}^{n+1}v^{\mathrm{s}}_{Ii}$ and ${}^{n+1}v^{\mathrm{fc}}_{Ii} = {}^{n+1}v^{\mathrm{s}}_{Ii}$. For pressure variable ${}^{n+1}p^{\mathrm{fc}}_{I}$, since the meshes of $\Omega^{\mathrm{f}*}$ and ${}^{n+1}\Omega^{\mathrm{fc}}$ are not coincident, we have to interpolate the pressure from the fluid mesh to the solid mesh (also the mesh of fictitious mesh).

When we solve the fictitious fluid using CBS from ${}^{n}t$ to ${}^{n+1}t$ without $f_i^{\mathrm{f,FSI}}$, the three steps becomes as following.

Step I: Calculation of the intermediate momentum keeps the same form as Eq. (37), and we have

$$\begin{aligned} M^{\mathrm{fc}}_{IJ}\frac{{}^{*}v^{\mathrm{fc}}_{Ji} - {}^{n}v^{\mathrm{fc}}_{Ji}}{\Delta t} &= -{}^{n}C^{\mathrm{f}}_{IJ}\,{}^{n}v^{\mathrm{fc}}_{Ji} - \frac{\Delta t}{2}{}^{n}K^{\mathrm{f}}_{IJ}\,{}^{n}v^{\mathrm{fc}}_{Ji} \\ &\quad -{}^{n}F^{\mathrm{fc}}_{Ii} + {}^{n}f^{\mathrm{fc},\tau}_{Ii} + {}^{n}f^{\mathrm{fc},g}_{Ii} \\ &= {}^{*}RHS^{\mathrm{fc}}_{Ii} + {}^{n}f^{\mathrm{fc},g}_{Ii} \end{aligned} \tag{44}$$

Step II: Calculation of pressure. The pressure is interpolated from ${}^{n+1}p^{\mathrm{f}}_{I}$ calculated on the fluid domain $\Omega^{\mathrm{f}*}$ using standard FEM interpolation as following.

$${}^{n+1}p^{\mathrm{fc}}_{I} = \sum_{J}\Phi^{\mathrm{f}}_{J}\left({}^{n+1}\mathbf{x}^{\mathrm{fc}}_{I}\right){}^{n+1}p^{\mathrm{f}}_{J} \tag{45}$$

where Φ^{f}_{J} is the shape function of fluid node J in the element which covers the fictitious particle (solid node). Therefore, we need to find the interaction pair from fluid to solid at each time step, and we will introduce that in the following section.

Step III: The momentum correction also keeps the same form as Eq. (39)

$$\begin{aligned} M^{\mathrm{fc}}_{IJ}\frac{{}^{n+1}\tilde{v}^{\mathrm{fc}}_{Ji} - {}^{n}v^{\mathrm{fc}}_{Ji}}{\Delta t} &= {}^{n+1}RHS^{\mathrm{fc}}_{Ii} \\ &= M^{\mathrm{fc}}_{IJ}\frac{{}^{*}v^{\mathrm{fc}}_{Ji} - {}^{n}v^{\mathrm{fc}}_{Ji}}{\Delta t} - G^{\mathrm{fc}}_{IJi}\,{}^{n+1}p^{\mathrm{fc}}_{J} \end{aligned} \tag{46}$$

In the above equation, ${}^{n+1}\tilde{v}^{\mathrm{fc}}_{Ji}$ is the calculated nodal velocity without FSI force $f_i^{\mathrm{f,FSI}}$. Apparently, ${}^{n+1}\tilde{v}^{\mathrm{fc}}_{Ji}$ is different from ${}^{n+1}v^{\mathrm{fc}}_{Ii} = {}^{n+1}v^{\mathrm{s}}_{Ji}$, and thus the FSI force $f_i^{\mathrm{f,FSI}}$ take effects to enforce the velocity condition (gravity force is ignored):

$$
\begin{aligned}
{}^{n+1}f_{Ii}^{\mathrm{f,FSI}} &= M_{IJ}^{\mathrm{fc}} \frac{{}^{n+1}v_{Ji}^{\mathrm{fc}} - {}^{n+1}\tilde{v}_{Ji}^{\mathrm{fc}}}{\Delta t} \\
&= M_{IJ}^{\mathrm{fc}} \frac{\left({}^{n+1}v_{Ji}^{\mathrm{fc}} - {}^{n}v_{Ji}^{\mathrm{fc}}\right) - \left({}^{n+1}\tilde{v}_{Ji}^{\mathrm{fc}} - {}^{n}v_{Ji}^{\mathrm{fc}}\right)}{\Delta t} \\
&= M_{IJ}^{\mathrm{fc}} \frac{\left({}^{n+1}v_{Ji}^{\mathrm{fc}} - {}^{n}v_{Ji}^{\mathrm{fc}}\right)}{\Delta t} - {}^{*}RHS_{Ii}^{\mathrm{fc}} + G_{IJi}^{\mathrm{fc}}\,{}^{n+1}p_{J}^{\mathrm{fc}}
\end{aligned} \tag{47}
$$

The FSI force on the solid part which serves as the external nodal force can solved explicitly as following:

$$
\begin{aligned}
{}^{n+1}f_{Ii}^{\mathrm{s,FSI}} &= -{}^{n+1}f_{Ii}^{\mathrm{f,FSI}} \\
&= -M_{IJ}^{\mathrm{fc}} \frac{\left({}^{n+1}v_{Ji}^{\mathrm{fc}} - {}^{n}v_{Ji}^{\mathrm{fc}}\right)}{\Delta t} - {}^{n}C_{IJ}^{\mathrm{f}}\,{}^{n}v_{Ji}^{\mathrm{fc}} \\
&\quad - \frac{\Delta t}{2}{}^{n}K_{IJ}^{\mathrm{f}}\,{}^{n}v_{Ji}^{\mathrm{fc}} - {}^{n}F_{Ii}^{\mathrm{fc}} + {}^{n}f_{Ii}^{\mathrm{fc},\tau} - G_{IJi}^{\mathrm{fc}}\,{}^{n+1}p_{J}^{\mathrm{fc}}
\end{aligned} \tag{48}
$$

4.3.2 Search the FSI pairs

Since the leaflets driven by blood move in a large range within the aortic valve, we need to find the FSI pairs for interpolation at every time step. During the computation, we have to find two types of FSI pairs: (1) the FSI pairs used to interpolate velocity from solid to fluid, i.e., find the fluid nodes covered by solid elements, denoted as S-F FSI pairs; and (2) the FSI pairs used to interpolate pressure from fluid to solid (fictitious fluid), i.e., find the solid nodes covered by fluid elements, denoted as F-S FSI pairs. For the FSI simulations of aortic valve, there are a large number of modes for both fluid and solid part, therefore, it will take extremely long time to search the FSI pairs if only the simple brute-force search is used.

The most distinguished feature of IS-FEM is that the fluid mesh keeps unchanged during the computation. This feature can greatly improve the searching efficiency since the data structure of the fluid mesh is also unchanged and only need to generate once at the beginning.

For the searching of F-S FSI pairs, we use the fastest known vicinity algorithm, named neighbor-to-neighbor scheme [50]. The shape functions (volumetric coordinates) are used to make the search jump from one element to its neighbor in a definite path. First, we need to get the adjacency information for each face in each element, i.e., to find the element indices on both sides of each face. In the IS-FEM, the fluid part is discretized using the tetrahedral elements, and thus for a solid node $\mathbf{x}_P^{\mathrm{s}}$, the shape function $\Phi_I^{\mathrm{f}}\left(\mathbf{x}_P^{\mathrm{s}}\right)$ can be calculated as

$$
\Phi_I^{\mathrm{f}}\left(\mathbf{x}_P^{\mathrm{s}}\right) = \frac{V_I\left(\mathbf{x}_P^{\mathrm{s}}\right)}{V} \tag{49}
$$

where V is the volume of fluid element, and $V_I\left(\mathbf{x}_P^{\mathrm{s}}\right)$ is the volume of the tetrahedral constituted of solid node and the fluid nodes of the element except node I. If the solid node is within the fluid element, we have

$$
\sum_{a=I,J,K,L} \Phi_a^{\mathrm{f}}\left(\mathbf{x}_P^{\mathrm{s}}\right) = 1 \text{ and } \Phi_a^{\mathrm{f}}\left(\mathbf{x}_P^{\mathrm{s}}\right) \geq 0 \tag{50}
$$

If the solid node is not within the current fluid element, the verification will be carried out for the next element which shares the face $J-K-L$ with

$$
\Phi_I^{\mathrm{f}}\left(\mathbf{x}_P^{\mathrm{s}}\right) = \min\left(\Phi_a^{\mathrm{f}}\left(\mathbf{x}_P^{\mathrm{s}}\right), a = I, J, L, K\right) \tag{51}
$$

The above equation indicates that the next element shares the face opposite to the node with minimal shape function. In the IS-FEM, the solid is fully immersed in the fluid (that means every solid node is covered by a corresponding fluid element) and moves in a continuous pattern, therefore, if we choose the element set in the previous step as the initial status for the search of F-S FSI pairs, it only needs 1 or 2 steps to find the next fluid element.

Although the neighbor-to-neighbor scheme is extremely fast, there are some limitations of this method. First, the adjacency information must be available. So it is suitable for the mesh with fixed topology or we have to design algorithm and data structure to update the adjacency information. Second, the method is especially suitable for the convex search domain. When the domain become concave or has gaps or holes, the method need a lot extra operations and become less efficient. Therefore, this method is not suitable to detect the S-F FSI pairs for the aortic valve simulation since the leaflets in the valve are concave, thin, and much smaller than the fluid domain.

In this research, we use a more general method, the octree search, to find the S-F FSI pairs. First, the octree is created using the coordinates of fluid nodes. The cube size at the finest level of the tree is determined by the size of the minimal fluid element to obtain an appropriate number of nodes in the cube. Then we loop all the solid elements to detect which fluid node is covered by the current element. For a fluid node $\mathbf{x}_P^{\mathrm{f}}$, we still use the Eq. (50) as the criterion. However, the shape function should be changed to $\Phi_I^{\mathrm{s}}\left(\mathbf{x}_P^{\mathrm{f}}\right)$ in the solid element at current configuration.

After the FSI pairs are obtained, the value at the covered node can be obtained using the standard FE interpolation as following:

$$
\begin{cases}
{}^{n+1}v_{Pi}^{\mathrm{f}} = \displaystyle\sum_{a=I,J,K,L} {}^{n+1}\Phi_a^{\mathrm{s}}\left(\mathbf{x}_P^{\mathrm{f}}\right){}^{n+1}v_{ai}^{\mathrm{s}} \\
{}^{n+1}p_P^{\mathrm{fc}} = \displaystyle\sum_{a=I,J,K,L} \Phi_a^{\mathrm{f}}\left(\mathbf{x}_P^{\mathrm{s}}\right){}^{n+1}p_a^{\mathrm{f}}
\end{cases} \tag{52}
$$

4.4 Full procedure of FSI simulation using IS-FEM

Now, we can summarize the procedure of IS-FEM as following.

(1) Preprocessor of IS-FEM

(1.1) Import mesh data of fluid and solid domain;

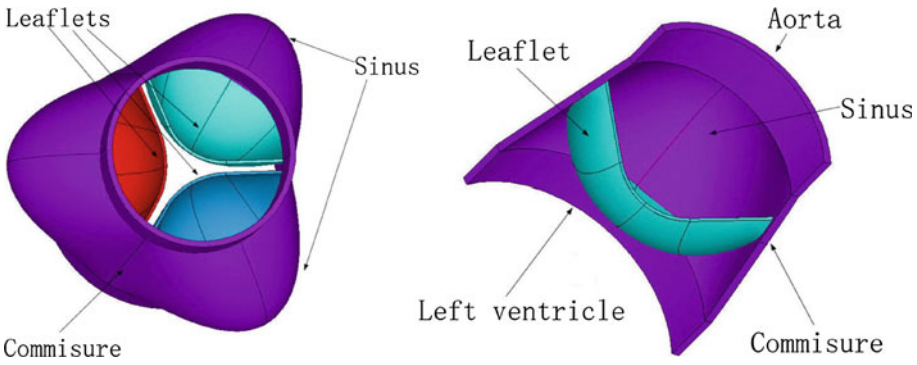

Fig. 3 Geometric model of an ideal aortic valve

(a) Full valve **(b)** 1/3 of the valve

(1.2) Calculate FE matrices for fluid: $\mathbf{M}^{\mathrm{f}}$, $\mathbf{H}^{\mathrm{f}}$, $\mathbf{\Phi}^{\mathrm{f}}$ and $\mathbf{\Phi}^{\mathrm{f}}_{,i}$;
(1.3) Calculate FE matrices for solid: $\mathbf{M}^{\mathrm{s}}$ and ${}^{0}\mathbf{B}_{I0}$;
(1.4) Create octree from fluid nodes for FSI searching;
(1.5) Obtain adjacency information from fluid elements for FSI searching;

(2) Set initial and boundary conditions for both fluid and solid.
(3) For each time step:

(3.1) Solid solver using central difference method with total Lagrangian description:

I. Update velocity and displacement at $t^{n+1/2}$

$$\begin{cases} (\mathbf{v}^{\mathrm{s}})^{n+1/2} = (\mathbf{v}^{\mathrm{s}})^{n} + \frac{\Delta t}{2}(\mathbf{a}^{\mathrm{s}})^{n} \\ (\mathbf{u}^{\mathrm{s}})^{n+1/2} = (\mathbf{u}^{\mathrm{s}})^{n} + \Delta t\,(\mathbf{v}^{\mathrm{s}})^{n} \\ (\mathbf{x}^{\mathrm{s}})^{n+1} = (\mathbf{x}^{\mathrm{s}})^{0} + (\mathbf{u}^{\mathrm{s}})^{n+1/2} \end{cases} \tag{53}$$

II. Calculate internal nodal forces $\mathbf{F}^{\mathrm{s,int}}$ at current configuration using equations in Sect. 3 (S-FEM for hyperelastic materials).
III. Detect contact and calculate contact force $\mathbf{F}^{\mathrm{s,contact}}$. The external nodal forces can be written as

$$\mathbf{F}^{\mathrm{s,ext}} = \mathbf{F}^{\mathrm{s,contact}} + \mathbf{F}^{\mathrm{s,FSI}} \tag{54}$$

IV. Calculate acceleration and velocity at t^{n+1}

$$\begin{cases} (\mathbf{a}^{\mathrm{s}})^{n+1} = (\mathbf{M}^{\mathrm{s}})^{-1}\left(\mathbf{F}^{\mathrm{s,ext}} - \mathbf{F}^{\mathrm{s,int}}\right) \\ (\mathbf{v}^{\mathrm{s}})^{n+1} = (\mathbf{v}^{\mathrm{s}})^{n+1/2} + \frac{\Delta t}{2}(\mathbf{a}^{\mathrm{s}})^{n+1} \end{cases} \tag{55}$$

V. Apply boundary conditions.

(3.2) Find FSI pairs at current configuration $(\mathbf{x}^{\mathrm{s}})^{n+1}$

I. Find F-S FSI pairs using neighbor-to-neighbor scheme;
II. Find S-F FSI pairs using octree search.

(3.3) CBS fluid solver

I. Interpolate FSI velocity conditions from solid results based on S-F FSI pairs;
II. Apply velocity and pressure boundary conditions;
III. Calculate $\left(\mathbf{v}^{\mathrm{f}}\right)^{n+1}$ and $\left(\mathbf{p}^{\mathrm{f}}\right)^{n+1}$ using CBS introduced in Sect. 4.1.

(3.4) Calculate FSI force

I. Prepare fictitious fluid mesh from solid mesh at current configuration;
II. Interpolate FSI pressure conditions from fluid results based on F-S FSI pairs;
III. Calculate FSI forces using Eq. (48) in Sect. 4.3.1.

(3.5) Update data for next time step.
(3.6) Postprocessor and write intermediate results if necessary.

(4) End of computation.

Table 1 Geometric parameters of aortic valve [9] (dimensions in mm)

r_b	r_c	h	r_{sm}	h_{sm}	h_s	L_h	L_t	W_t
11.75	9.10	17.8	13.3	10.0	18.33	16.0	0.3	1.0

r_b radius at the base of the valve, r_c radius at the commissures, h valve height, r_{sm} maximum radius of aortic sinus, h_{sm} height at r_{sm}, L_h leaflet height, L_t leaflet thickness, W_t valve wall thickness

This is a weakly-coupled FSI coupling algorithm. Although strongly-coupled algorithms such as block-iterative coupling, quasi-direct coupling, or direct coupling algorithms (see [51] for the terminology and the algorithms), might be needed depending on how light the structure is compared to the fluid masses involved in the FSI dynamics, in our case here we find the weakly-coupled algorithm sufficient.

5 FSI simulation of aortic valve

5.1 FE model of aortic valve

An 3D ideal model of aortic valve is shown in Fig. 3. The ideal aortic valve is modeled as three identical leaflets with

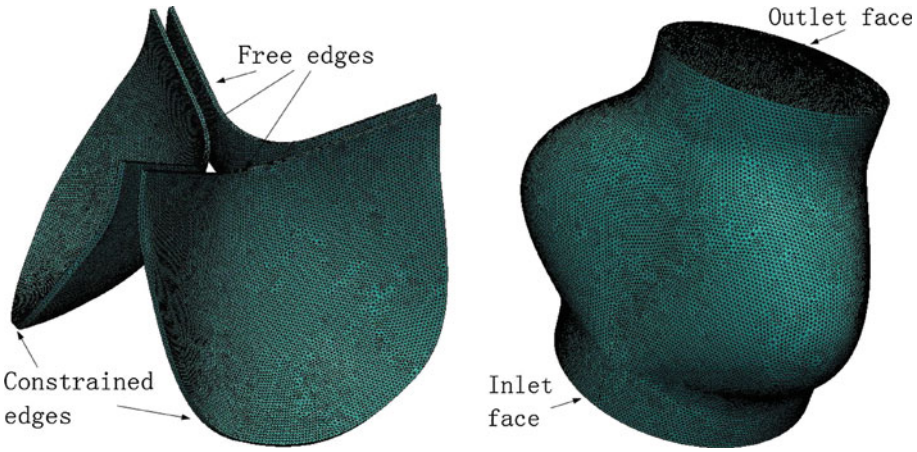

(a) Leaflets at initial configuration **(b)** Fluid mesh of valve

Fig. 4 Unstructured tetrahedral mesh of leaflets and valve. There are two layers of solid elements for each leaflet including 23,391 nodes and 121,576 elements, and 185,679 nodes and 986,893 elements for the fluid domain

Table 2 Parameters for FSI simulation of aortic valve opening

ρ^s	c_{10}	c_{01}	κ	ρ^f	μ^f	p_{inlet} [a]	p_{outlet} [a]
1,000 kg/m^3	1,000 Pa	200 Pa	$50c_{10}$	1,000 kg/m^3	0.1 Pa s	120 mmHg	80 mmHg

[a] The pressure load is simplified as constant

uniform thickness and their corresponding sinuses. Since contact between leaflets may occur during moving, we still have to use the full model to carry out the simulation. The modeling method is the same as in [9,52]. The size parameters are listed in Table 1.

Since the IS-FEM is used here, there is no need to generate the body-fitted meshes. The leaflets (solid part) and the valve (fluid part) are separately discretized using tetrahedral elements as shown in Fig. 4. In this paper, the valve wall is treated as solid wall, and thus its thickness is ignored, and the fluid domain is bounded by its inner surfaces. The inlet face is defined as connecting to the left ventricle, and the outlet face is defined as connecting to the aorta. The leaflets are fixed to the valve wall using Dirichlet conditions imposed over the constrained edges. To better simulate the large bending deformations, we use two layers of tetrahedral elements to discretize the leaflets.

5.2 Simulation of aortic valve opening

The aortic valve opens and closes according to the blood pressure difference between the left ventricle and the aorta. During ventricular systole, pressure rises in the left ventricle. When the pressure in the left ventricle rises above the pressure in the aorta, the aortic valve opens, allowing blood to exit the left ventricle into the aorta. In this paper, the opening of aortic valve is numerically simulated using the IS-FEM. The material parameters for leaflets and blood, and the pressure load for the simulation are listed in Table 2. It should be noted that we focus here on the development and application of IS-FEM to study the FSI phenomena in aortic valve rather than on the accurate approximation of the physiological situation, which will be investigated in another paper in the near future.

At the initial state, both the blood and the leaflets are stationary, and the blood is driven by the pressure difference between inlet and outlet faces. The time step length for non-contact situation is 5.0E−6s, and when contact occurs between two leaflets or between leaflets and the valve wall, the time step length becomes 2.5E−6s.

The fluid results on a symmetry plane of the valve and corresponding opening positions of leaflets of five successive time points are shown in Fig. 5. The slender light blue stripe in the figures denotes the immersed leaflet at current configuration, and the leaflets are colored by the magnitudes of velocities of solid nodes. Figure 6 shows the stream lines within 1/3 valve and deformations of one leaflet. The Reynolds number, defined as $Re = 2\rho^f v^f r_c/\mu^f$, reaches 700 at peak velocity at t = 1.9E−2s, the final opening position. This number is much lower than the physiological value which reads $Re \approx 4000$ (turbulent flow). The reason for this difference is that a larger viscosity coefficient and coarse meshes are chosen such that the computational time is resonable and keep the flow as laminar (since there is no turbulence model considered in the current version of CBS) to demonstrate the proposed IS-FEM.

From computational results shown in Fig. 5 (2D presentation) and Fig. 6 (3D presentation), we can see

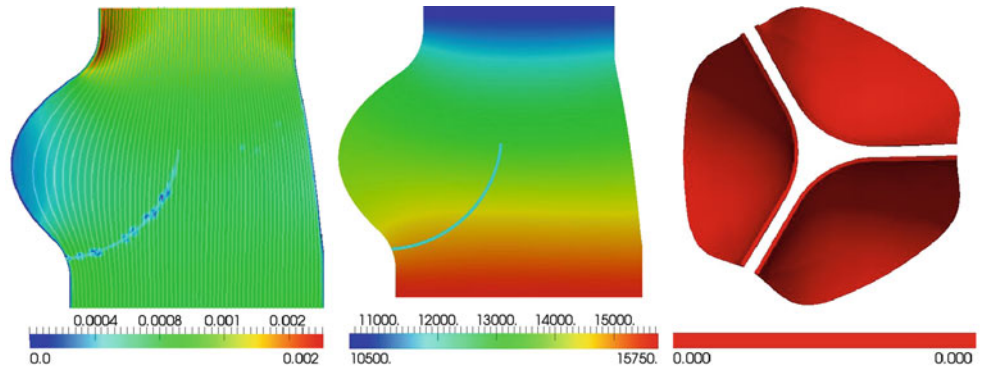

(a) t=5.0E-6s

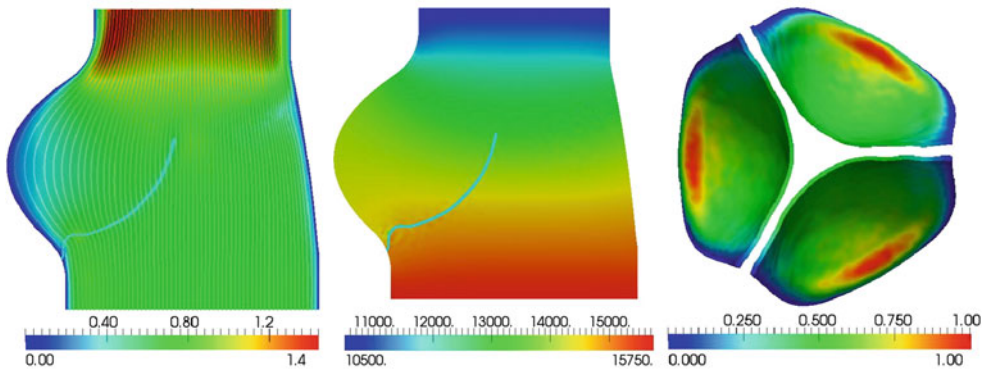

(b) t=5.0E-3s

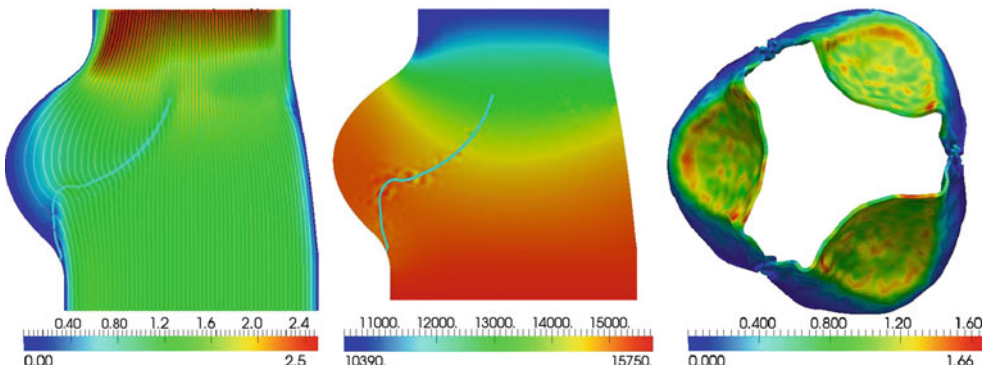

(c) t=1.0E-2s

Fig. 5 Velocity (with stream lines on slice) and pressure contours of a symmetry plane of the valve and their corresponding opening positions at different time steps

(1) The leaflets are driven aside to the sinuses under the pressure difference between the inlet and outlet faces. And therefore the blood in the sinuses are pushed out due to the movement of the leaflet, see Fig. 5c, d.
(2) The streamlines of blood curves more severely at both sides of the leaflets since the velocity at the nodes covered by the solid elements are interpolated from solid nodes to impose the FSI conditions rather than computed from the fluid equations.
(3) The pressure distribution near the leaflets is less smooth than the other area also since the FSI conditions are imposed. Moreover, the pressure distributions on the

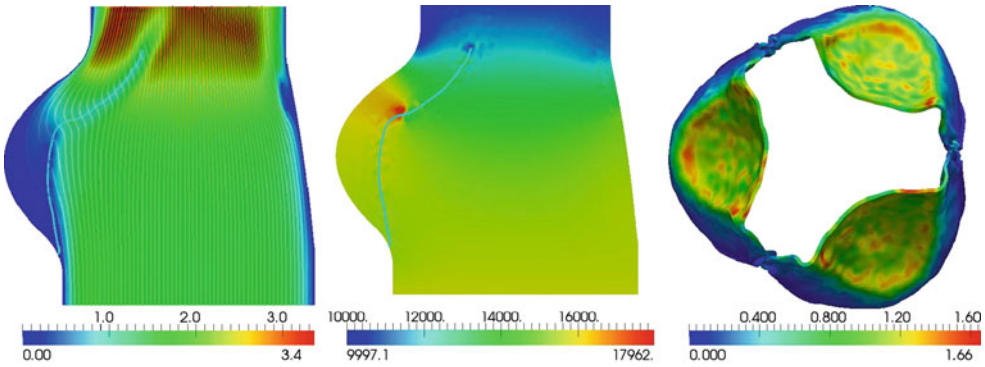

(d) t=1.5E-2s

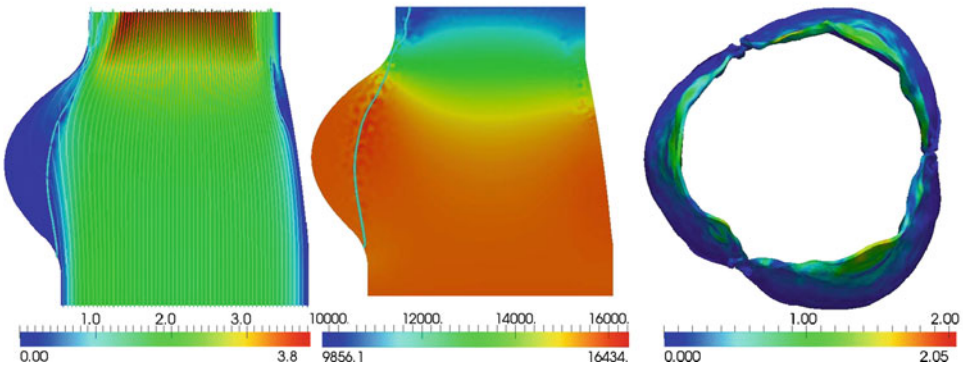

(e) t=1.9E-2s

Fig. 5 continued

leaflet surfaces are obviously non-uniform. Therefore, only applying uniform pressure loads is not accurate enough to obtain the stresses and deformations of leaflets.

(4) It seems like the leaflet becomes longer during the opening process. However, the leaflet does not actually become longer, it only drifts forward and becomes flat during movement.

(5) Since the contacts between the leaflets and between the leaflets and rigid fluid wall are considered, no penetration is observed in the simulation results.

Figure 7 shows the deformations of one leaflet during the opening process at the six successive time points same as in Figs. 5 and 6, and the leaflet is colored by the magnitude of displacements. In this figure, it is clearly shown that the leaflet drifts forward with the blood flow and move outward in the radial direction. The curvatures of the leaflets reverse gradually from the bottom to the top, and the three leaflets form a non-concave geometry at the final opening position.

6 Conclusion

A 3D IS-FEM is developed and applied to the FSI simulations of aortic valves. The interactions between the blood and the hyperelastic leaflets are realized by calculating FSI forces based on a set of Lagrangian fictitious fluid mesh, which is coincides with the moving solid mesh, and there is no need to use a body-fitted mesh. The fluid and solid domains are solved separately. In this work, the fluid domain is solved by CBS method on a fixed mesh. According to the general formulations of IS-FEM introduced in Sect. 2, we can solve the fluid domain using the other numerical schemes. The solid domain is solved using smoothed finite element method, which is extremely suitable for solving the hyperelastic materials with large deformation. Both the

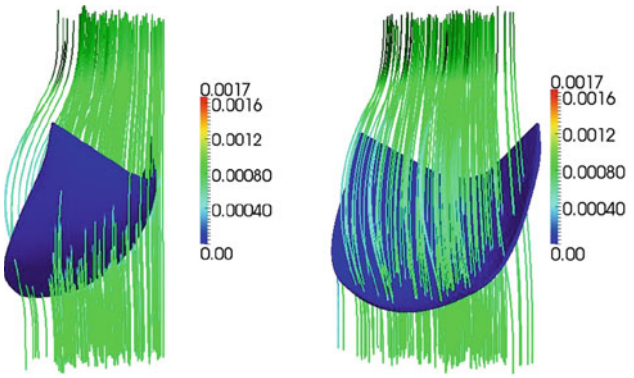

(a) t=5.0E-6s

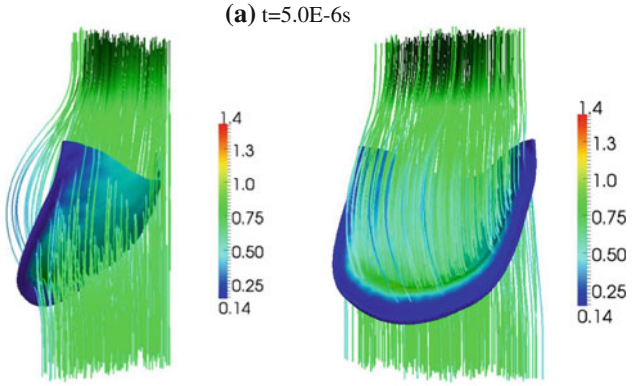

(b) t=5.0E-3s

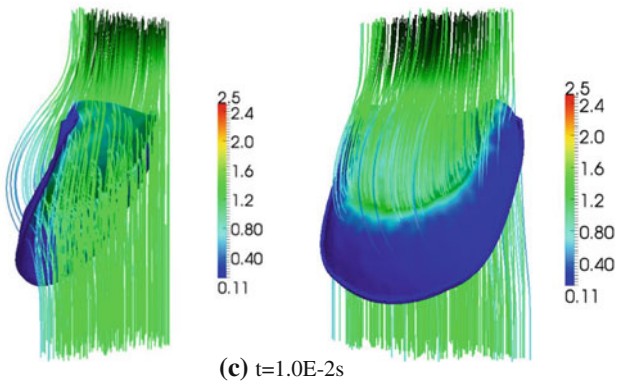

(c) t=1.0E-2s

Fig. 6 Streamlines of 1/3 valve

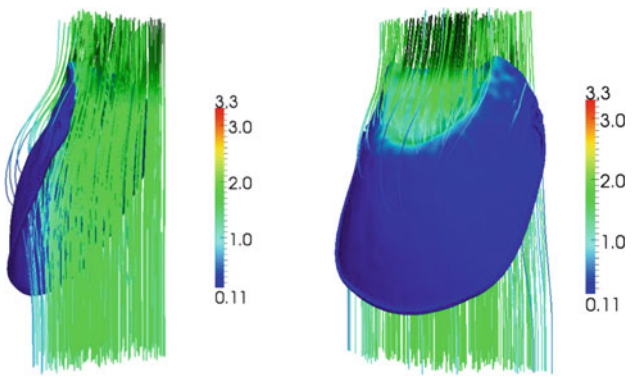

(d) t=1.5E-2s

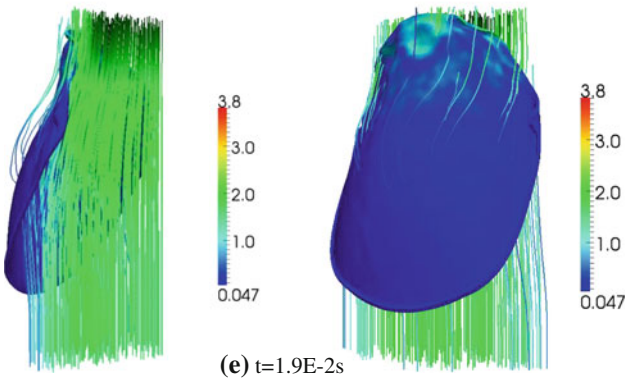

(e) t=1.9E-2s

Fig. 6 continued

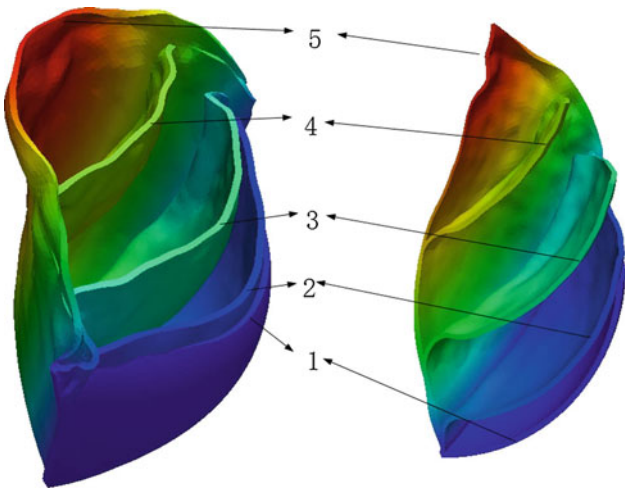

Fig. 7 Deformations of one of the leaflets (the numbers denote the time points same as in Figs. 5 and 6)

fluid and the solid domains are discretized using tetrahedral elements, which greatly simplify the mesh generation process.

An ideal aortic valve model is constructed and its opening process is simulated using the proposed IS-FEM. Although some data for the simulation are non-physiological, the valve deformations and blood velocities (magnitude and distribution) are comparable with numerical investigation previously done. This means IS-FEM is capable of simulating the aortic valve dynamics coupled with hemodynamics, and could provide accurate results if the physiological data are available. This method can be potentially used as an efficient numerical tool to provide surgical plan based on the detailed valve dynamics of the patient-specific aortic valve.

References

1. Rosamond W, Flegal K et al (2008) Heart disease and stroke statistics—2008 update: a report from the American Heart Association

Statistics Committee and Stroke Statistics Subcommittee. Circulation 117(4):e25–e146
2. Lloyd-Jones D, Adams RJ et al (2010) Heart disease and stroke statistics—2010 update: a report from the American Heart Association. Circulation 121(4):e135
3. Roger VL, Go AS et al (2012) Heart disease and stroke statistics—2012 update: a report from the American Heart Association. Circulation 125(4):e122–e130
4. Yacoub MH, Takkenherg JJ (2005) Will heart valve tissue engineering change the world?. Nat Clin Pract Cardiovasc Med 2: 60–61
5. Bonow RO et al (2006) ACC/AHA 2006 guidelines for the management of patients with valvular heart disease: a report of the American College of Cardiology/American Heart Association Task Force on Practice Guidelines (writing committee to revise the 1998 Guidelines for the Management of Patients With Valvular Heart Disease): developed in collaboration with the Society of Cardiovascular Anesthesiologists: endorsed by the Society for Cardiovascular Angiography and Interventions and the Society of Thoracic Surgeons. Circulation 114:e84–e231
6. Subramanian S, Borger MA (2010) Aortic valve reconstruction: current status. Herz 35:88–93
7. Croft LR, Mofrad MRK (2010) Computational modeling of aortic heart valves, Chap. 7. In: De S, Guilak F, Mofrad MRK (eds) Computational modeling in biomechanics. Springer, New York
8. Labrosse MR, Lobo K, Beller CJ (2010) Structural analysis of the natural aortic valve in dynamics: from unpressurized to physiologically loaded. J Biomech 43:1916–1922
9. Labrosse MR, Boodhwani M, Sohmer B, Beller CJ (2011) Modeling leaflet correction techniques in aortic valve repair: A finite element study. J Biomech 44:2292–2298
10. Grande-Allen KJ et al (2001) Finite-element analysis of aortic valve-sparing: influence of graft and stiffness. IEEE Trans Biomed Eng 48:647–659
11. Howard IC, Patterson EA, Yoxall A (2003) On the opening mechanism of the aortic valve: some observations from simulations. J Med Eng Technol 27:259–266
12. Hughes TJR, Liu WK, Zimmermann TK (1981) Lagrangian-Eulerian finite element formulation for incompressible viscous flows. Comput Methods Appl Mech Eng 29:329–349
13. Donea J, Giuliani S, Halleux JP (1982) An arbitrary Lagrangian-Eulerian finite element method for transient dynamic fluid-structure interactions. Comput Methods Appl Mech Eng 33:689–723
14. Tezduyar TE (1992) Stabilized finite element formulations for incompressible flow computations. Adv Appl Mech 28:1–44
15. Tezduyar TE, Sathe S (2007) Modeling of fluid-structure interactions with the space-time finite elements: solution techniques. Int J Numer Methods Fluids 54:855–900
16. Takizawa K, Tezduyar TE (2011) Multiscale space-time fluid–structure interaction techniques. Comput Mech 48:247–267
17. Takizawa K, Tezduyar TE (2012) Space-time fluid-structure interaction methods. Math Model Methods Appl Sci 22:1230001
18. Tezduyar TE, Aliabadi S, Behr M, Johnson A, Mittal S (1993) Parallel finite element computation of 3D flows. Computer 26:27–36
19. Johnson AA, Tezduyar TE (1994) Mesh update strategies in parallel finite element computations of flow problems with moving boundaries and interfaces. Comput Methods Appl Mech Eng 119:73–94
20. Stein K, Tezduyar TE, Benney R (2003) Mesh Moving Techniques for Fluid-Structure Interactions with Large Displacements. J Appl Mech 70:58–63
21. Stein K, Tezduyar TE, Benney R (2004) Automatic Mesh Update with the Solid-Extension Mesh Moving Technique. Comput Methods Appl Mech Eng 193:2019–2032
22. Johnson AA, Tezduyar TE (1999) Advanced Mesh Generation and Update Methods for 3D Flow Simulations. Comput Mech 23:130–143
23. Takizawa K, Spielman T, Tezduyar TE (2011) Space-time FSI modeling and dynamical analysis of spacecraft parachutes and parachute clusters. Comput Mech 48:345–364
24. Bazilevs Y, Hsu MC, Takizawa K, Tezduyar TE (2012) ALE-VMS and ST-VMS methods for computer modeling of wind-turbine rotor aerodynamics and fluid-structure interaction. Math Model Methods Appl Sci 22:1230002
25. Takizawa K, Bazilevs Y, Tezduyar TE (2012) Space-time and ALE-VMS techniques for patient-specific cardiovascular fluid-structure interaction modeling. Arch Comput Methods Eng 19:171–225
26. Tezduyar TE, Takizawa K, Moorman C, Wright S, Christopher J (2010) Multiscale sequentially-coupled arterial FSI technique. Comput Mech 46:17–29
27. Takizawa K, Moorman C, Wright S, Christopher J, Tezduyar TE (2010) Wall shear stress calculations in space-time finite element computation of arterial fluid-structure interactions. Comput Mech 46:31–41
28. Torii R, Oshima M, Kobayashi T, Takagi K, Tezduyar TE (2010) Role of 0D peripheral vasculature model in fluid-structure interaction modeling of aneurysms. Comput Mech 46:43–52
29. Moireau P, Xiao N, Astorino M et al (2012) External tissue support and fluid-structure simulation in blood flows. Biomech Model Mechanobiol 11:1–18
30. Morsi YS, Yang WW, Wong CS, Das S (2007) Transient fluid-structure coupling for simulation of a trileaflet heart valve using weak coupling. J Artif Organs 10:96–103
31. Marom G, Haj-Ali R, Raanani E et al (2012) A fluid-structure interaction model of the aortic valve with coaptation and compliant aortic root. Med Biol Eng Comput 50:173–182
32. Peskin CS (1977) Numerical-analysis of blood-flow in heart. J Comput Phys 25(3):220–252
33. Peskin CS, McQueen DM (1995) A general method for the computer simulation of biological systems interacting with fluids. Sym Soc Exp Biol 49:265–276
34. Peskin CS (2002) The immersed boundary method. Acta Numer 11:479–517
35. Griffith BE, Luo X, Mc McQueen DM, Peskin CS (2009) Simulating the fluid dynamics of natural and prosthetic heart valves using the immersed boundary method. Int J Appl Mech 1(1):137–177
36. De Hart J, Peters GW, Schreurs PJ, Baaijens FP (2000) A two-dimensional fluid-structure interaction model of the aortic valve. J Biomech 33:1079–1088
37. De Hart J, Peters GW, Schreurs PJ, Baaijens FP (2003) A three-dimensional computational analysis of fluid-structure interaction in the aortic valve. J Biomech 36:103–112
38. De Hart J, Peters GW, Schreurs PJ, Baaijens FP (2004) Collagen fibers reduce stresses and stabilize motion of aortic valve leaflets during systole. J Biomech 37:303–311
39. Zhang L, Gerstenherger A, Wang X, Liu WK (2004) Immersed finite element method. Comput Methods Appl Mech Eng 193:2051–2067
40. Liu WK, Liu Y, Farrell D et al (2006) Immersed finite element method and its applications to biological systems. Comput Methods Appl Mech Eng 195:1722–1749
41. Zhang LT, Gay M (2007) Immersed finite element method for fluid-structure interactions. J Fluid Struct 23:839–857
42. Zhang ZQ, Yao JY, Liu GR (2011) An immersed smoothed finite element method for fluid-structure interaction problems. Int J Comput Methods 8(4):747–757
43. Zhang ZQ, Liu GR, Khoo BC (2012) A three dimensional immersed smoothed finite element method (3D IS-FEM) for

fluid-structure interaction problems. Comput Mech. doi:10.1007/s00466-012-0710-1
44. Liu GR, Nguyen-Thoi T, Lam KY (2009) An edge-based smoothed finite element method (ES-FEM) for static, free and forced vibration analyses of solids. J Sound Vib 320(4–5):1100–1130
45. Nguyen-Thoi T, Liu GR, Lam KY, Zhang GY (2009) A face-based smoothed finite element method (FS-FEM) for 3D linear and geometrically non-linear solid mechanics problems using 4-node tetrahedral elements. Int J Numer Methods Eng 78:324–353
46. Liu GR, Nguyen-Thoi T (2010) Smoothed finite element methods. CRC Press,
47. Zienkiewicz OC, Tayler RL (2000) The finite element method, Vol. 3: Fluid dynamics, 5 edn. Butterworth-Heinemann, Oxford
48. Zienkiewicz OC, Nithiarasu P, Codina R et al (1999) The characteristic-based-split procedure: an efficient and accurate algorithm for fluid problems. Int J Numer Methods Fluids 31(1):359–392
49. Nithiarasu P, Mathur JS, Weatherill NP, Morgan K (2004) Three-dimensional incompressible flow calculations using the characteristic based split (CBS) scheme. Int J Numer Methods Fluids 44:1207–1229
50. Löhner R (1995) Robust, vectorized search algorithm for interpolation on unstructured grids. J Comput Phys 118:380–387
51. Tezduyar TE, Sathe S, Keedy R, Stein K (2006) Space-time finite element techniques for computation of fluid-structure interactions. Comput Methods Appl Mech Eng 195:2002–2027
52. Labrosse MR, Beller CJ, Robicsek F, Thubrikar MJ (2006) Geometric modeling of functional trileaflet aortic valves: development and clinical applications. J Biomech 39:2665–2672